

## Highlights

### **Title 3: A Machine Learning Approach to Automate Ductile Damage Parameter Selection in Finite Element Simulations**

A.N. O'Connor, P.G. Mongan, N.P. O'Dowd

- Bayesian optimization derived parameters provide excellent agreement comparing simulated and experimental data.
- Ductile damage parameters are successfully derived for ambient and higher test temperatures.
- Required user-defined input such as test data can be easily generated from basic engineering tests.

# Title 3: A Machine Learning Approach to Automate Ductile Damage Parameter Selection in Finite Element Simulations

A.N. O'Connor<sup>a,b</sup>, P.G. Mongan<sup>a,c</sup>, N.P. O'Dowd<sup>a,b,c</sup>

<sup>a</sup>*School of Engineering, University of Limerick, Ireland*

<sup>b</sup>*Bernal Institute, University of Limerick, Ireland*

<sup>c</sup>*Confirm Smart Manufacturing Research Centre, Ireland*

---

## Abstract

A key limitation of finite element analysis is accurate modelling of material damage. While additional material models exist that improve correlations between simulated damage and experimental data, these models often require additional parameters that are difficult to estimate. In this work we show that Bayesian optimization, a machine learning technique, can be used to identify material model parameters. We show that Bayesian derived material model parameters result in simulated output with less than 2 % error compared to experimental data. The framework detailed here is fully autonomous, requiring only basic information that can be derived from a simple uni-axial tensile test. We have successfully applied this framework to three datasets of P91 material tested at ambient (20 °C) and higher (500 °C) temperatures.

*Keywords:* machine learning; bayesian optimization; ductile damage; parameter selection;

---

*Email address:* `alison.oconnor@ul.ie` (A.N. O'Connor)

## 1. Introduction

Many engineering datasets consist of experimental test data that are limited. Generating experimental data may be impossible due to lack of material or cost prohibitive for various reasons. There are some basic engineering tests that are commonly conducted to investigate material behaviour, one such is the uni-axial tensile test. The uni-axial tensile test is a standard test method that provides basic engineering information about a material's performance. It is used extensively throughout multiple industries as it requires little material and is relatively inexpensive.

FE modelling has been used extensively in engineering to solve a wide range of complex physics based problems including the assessment of structural performance [1-3]. In cases where experimental data are limited Finite Element (FE) simulations are often used to support hypotheses that cannot be experimentally investigated. In FEM complex geometries are discretized into small, simple shapes called elements. Partial differential equations are formulated for each element of the model and later re-combined to obtain a total solution for the geometry in question. FEM offers a level of detail not obtainable from analytical solutions but is relatively computationally expensive. Computational expense grows as one increases the model complexity.

The FE method can be applied to both linear and non-linear loading conditions but has some limitations in terms of material behaviour. One of the key limitations of FE methods is modelling material damage. Ductile damage modelling is a mathematical method typically applied to finite element simulations to improve the correlation between simulated and experimental behaviour under high strain conditions [4-6]. Essentially ductile

damage modelling more accurately represents material degradation effects compared to general simulation results. These damage material models are often complex, requiring parameters that are difficult to derive experimentally or analytically.

Machine learning methods offer a promising solution to solving complex multi-interaction problems. Predictive algorithms, informed directly by experimental and/or simulation data, have been successfully employed to solve numerous engineering problems across a wide range of industries [7–9]. Bayesian optimization (BO) has been shown to outperform other machine learning algorithms in solving black-box optimization problems [10]. BO is commonly used in machine learning for artificial neural network (ANN) hyperparameter selection [7, 11–13]. A major drawback of ANNs is the requirement of large datasets used for ANN model training [14] as this inherently implies that a significant dataset be generated for model training. Additionally, ANNs often require significant computing power and their predictive capabilities are limited by the size and quality of the training dataset [15, 16]. Ryan et al. [17] recently applied BO to directly solve function parameter values thus bypassing the requirement of an ANN completely. Machine learning has been previously applied to derive material damage model parameter values but these have typically involved the use of ANN's [4, 5, 18, 19] and a significant number of FE simulations. In this work we demonstrate how BO can be used to identify the material damage model parameters. The material damage model parameters derived in this work result in simulation data that closely matches experimental test data. The purpose of this work is to reduce the time, and thus the cost, associated with deriving difficult to

assess parameter values.

## 2. Material behaviour in FE simulations

~~FE simulations are commonly used to enhance limited experimental datasets.~~  
A key input to a FE simulation is test data that describes the material behaviour and this is typically defined by conducting uni-axial tensile testing. ~~At test temperatures exceeding ambient temperature failure of the tensile specimen occurs via ductile damage. Ductile damage, a common failure mechanism for high temperature operating conditions, is essentially failure by cavitation and/or plastic collapse [20, 21].~~ A uni-axial tensile testing consists of a standardised specimen geometry that is loaded in tension until complete separation of the specimen. Data are typically expressed in terms of engineering stress and strain, where stress and strain are ~~analytically~~ derived from test measurements of applied load and specimen displacement. For metals the relationship between stress and strain comprises three regions: a linear region demonstrating the elastic properties, a work hardening region where stress increases non-linearly with strain, and a necking region where stress decreases non-linearly with increasing strain. Several key mechanical properties derived from a tensile test and the three regions of interest are illustrated in Figure 1. The yield strength ( $\sigma_y$ ) defines the point at which material behaviour ~~changes from elastic to plastic deformation.~~ The linear region comprises data preceding the yield point of the material and the materials stiffness, ~~it's~~ Young's modulus ( $E$ ), is calculated from linear data as shown in Figure 1. ~~Once plastically deformed (i.e. beyond  $\sigma_y$ ) the specimen geometry begins to change~~ and a local geometrical discontinuity known as

a ‘neck’ forms. The maximum load bearing capacity, also known as the ultimate tensile strength  $\sigma_{UTS}$ , denotes the point beyond which the materials load bearing capacity degrades. The strain hardening region occurs within the bounds of  $\sigma_y \leq \sigma \leq \sigma_{UTS}$  as illustrated in Figure 1 and depicts an increasing non-linear stress-strain relationship. As you continue stretching the material voids nucleate around the larger particulates such as precipitates and carbides [21]. As more voids nucleate, those already in existence grow larger. Eventually larger voids will begin to interact with one another forming micro-cracks that begin to degrade the performance of the material ( $\sigma_{UTS}$ ). Over time the micro-cracks coalesce resulting in specimen failure (i.e. complete separation of the specimen into two parts). Generally specimen failure occurs at the necked region due to the higher stresses and triaxial conditions located around the local geometrical discontinuity [20]. It is common in en-

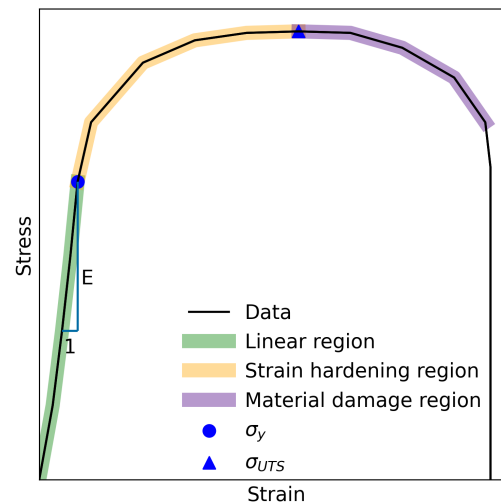


Figure 1: Illustration depicting material behaviour during uni-axial tensile test experiment.

gineering applications to convert load-displacement test data to stress-strain

~~data using analytically defined relationships. The analytical conversion from load-displacement to stress-strain assumes that the specimen geometry seen at the initial stages of testing does not change. This is of course not true because once the specimen has been plastically deformed and a ‘neck’ is formed the geometry is no longer identical to that of an undamaged specimen. To account for this local geometrical discontinuity, the stress-strain relationship applied in FE simulations must be further modified to a true stress-true strain relationship. The conversion from engineering stress-strain to true stress-true strain occurs analytically. However, the analytical expression is valid only up to the maximum load bearing capacity ( $\sigma_{UTS}$ ) and so data beyond  $\sigma_{UTS}$  must be discarded. To ensure FE simulations continue beyond the  $\sigma_{UTS}$  point users must manually define the material behaviour. Often the assumed true stress-true strain behaviour is only moderately successful in improving the simulated outcomes compared to experimental data in the material degradation region.~~

In this work we have assumed a linear relationship beyond  $\sigma_{UTS}$ . The linear relationship between true stress-true strain can be defined by a single parameter,  $m$ , describing the slope of the line. ~~The value of parameter  $m$  is not explicitly defined by the user, it is a parameter that the Bayesian optimization framework aims to find.~~

### 2.1. The damage model

~~To improve simulated damage additional material models are applied to more accurately represent material degradation effects as illustrated in Figure 2. One of the more popular material models for predicting damage in FE simulations is the Gurson-Tvergaard-Needleman (GTN) model [5, 22] that~~

was mathematically derived based on the physics of crystalline structures [6]. The GTN model is a yield criterion which depends on the deformation history of each element in an FE simulation [23]. The GTN model parameters dictate the rate of material degradation but these values are not easily definable as some parameters are considered potentially ‘strongly coupled’ [6]. Most previous studies assume several GTN parameter values to be fixed based on unit cell analyses conducted by Zhang et al. [6], Tvergaard and Needleman [23]. Other parameter values can be determined experimentally, though these methods are somewhat subjectively analysed [6, 22], leading to large variations in data. Indicative values have been provided by others [21, 22], but significant user input is required to ascertain parameter values that will provide a simulation result that mimics experimental data. Any remaining parameters are typically estimated based on manually iterating the relevant parameter value/(s), conducting numerical simulations and matching the simulation result to experimental data. This iterative parameter selection process is sometimes referred to as the inverse FE method. Apart from this method being labour intensive it may not be possible to find a unique set of parameters given the coupling effects [6] between various parameters. This is inefficient, arduous and subject to human error.

A 1-dimensional description of the GTN model is described in Equation 1. Where  $\sigma$  describes the current stress state of each element,  $\sigma_y$  is the material yield strength,  $f$  is the current void volume fraction and  $q_1$ ,  $q_2$ , and  $q_3$  are fitting parameters.

$$\frac{\sigma}{\sigma_y} + 2q_1f \left( \cos \left( \frac{q_2\sigma}{2\sigma_y} \right) \right) - q_3f^2 - 1 = 0 \quad (1)$$

For stresses lower than the yield stress the material ( $\sigma < \sigma_y$ ) the



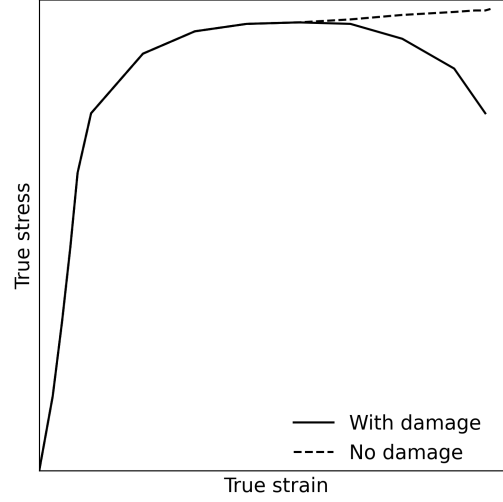


Figure 2: Illustration demonstrating the impact of additional material models on simulated material behaviour.

material behaviour is defined as shown in Equation 2 where  $E$  is the material stiffness and  $\epsilon$  is the applied strain.



$$\sigma = E\epsilon \quad (2)$$

Once plastic deformation has occurred ( $\sigma > \sigma_y$ ) the stress-strain relationship can be defined as shown in Equation 3 where  $A$  represents the yield offset and  $n$  the hardening behaviour of the material.

$$\sigma = A\epsilon^n \quad (3)$$

The void volume fraction,  $f$ , is described as detailed in Equation 4 where  $\dot{f}_n$  represents and  $\dot{f}_g$  represent the instantaneous void nucleation and growth, respectively. Void growth  $\dot{f}_g$ , Equation 6, is based on the law of conservation of mass where  $\dot{\epsilon}$  represents the instantaneous plastic strain. Void nucleation



$\dot{f}_n$ , Equation 5 is a normally distributed function with a mean  $\epsilon_N$  and standard deviation  $S_N$ . The nucleated void volume fraction  $\dot{f}_N$  is assumed to only increase under tensile loading conditions.  $\dot{\epsilon}$  represents the change in plastic strain while  $\bar{\epsilon}_m$  represents the equivalent plastic strain.

$$\dot{f} = \dot{f}_n + \dot{f}_g \quad (4)$$

$$\dot{f}_n = \frac{f_N}{S_N \sqrt{2\pi}} \exp \left[ -\frac{1}{2} \left( \frac{\bar{\epsilon}_m - \epsilon_N}{S_N} \right)^2 \right] \dot{\epsilon} \quad (5)$$


$$\dot{f}_g = (1 - f) \dot{\epsilon} \quad (6)$$

For most crystalline materials the initial void volume fraction of the material is non-zero [24]. The initial void volume fraction  $f_0$  relates to our void volume fraction  $f$  through the following:  $f = 1 - f_0$ . Hence, there are a total of 7 parameters in the GTN ductile damage model that we aim to fit using the BO framework:  $q_1$ ,  $q_2$ ,  $q_3$ ,  $S_N$ ,  $f_N$ ,  $\epsilon_N$ , and  $f_0$ .

### 3. The Bayesian Optimization Framework

From a mathematical perspective the objective of BO is to find the global minimum of an unknown function. Unknown functions, often referred to as black-box functions, mean that little or no information is available about the shape or characteristics of the function. There are two key ingredients to a BO framework: a probabilistic model and a loss function. The probabilistic model, sometimes called a surrogate model, describes our beliefs about the function based on observed data. The loss function describes whether

our previously observed data are optimised (i.e. converging towards a global minimum) [25]. To generate a surrogate model some observed data about the function must be provided to the BO framework. These data are then generalised using Gaussian Process Regression (GPR). The GPR is a collection of random variables that have consistent, joint Gaussian distributions that are completely specified by the mean and covariance function [26, 27]. The covariance function (also referred to as kernel, covariance kernel or kernel function), is user-defined and has significant impact on the GPR output, and by extension the overall BO result [28]. ~~It is the covariance function that controls key function properties (e.g. shape, smoothness, characteristic length scale of oscillations etc.).~~ For black-box functions where the shape and characteristics are unknowable it is common to combine multiple covariance functions to provide a wide-range of potential characteristics that might be relevant to our black-box function. ~~Readers are referred to [26, 27, 29] for more in-depth discussions of specific types of covariance functions and their influence on GPR output.~~

The probability distribution generated by the GPR is based on a ranking system, where input  $x$  is evaluated  $f(x)$ . The evaluation is then ranked in terms of its performance relative to the objective, this is often called the loss function. In this work the objective is to minimise the difference between a simulation and an experiment. To minimise our loss function we use the L-BFGS-B optimization  algorithm. The L-BFGS-B algorithm is popular for large scale optimization problems as it requires less memory compared to other methods. The algorithm uses historical gradient evaluations to build up an approximation of the objective function. ~~The L-BFGS-B algorithm~~

~~is considered relatively stable, has fewer control parameters than alternative methods and is computationally inexpensive [30].~~

Ranking our data and using historical information to select a new expensive evaluation point implemented through a specific ‘acquisition’ function.

The purpose of the acquisition function is to use data gathered thus far to identify an appropriate new evaluation point for our expensive evaluation method. The framework presented here iterates until either a suitable solution has been found or, some maximum number of iterations has been achieved.

In this work we are interested in defining values for 8 parameters related to material behaviour. One parameter ( $m$ ) describes the material behaviour beyond the ultimate tensile strength of the material (see Section 2), the remaining seven parameters ( $q_1$ ,  $q_2$ ,  $q_3$ ,  $S_N$ ,  $\epsilon_N$ ,  $f_N$  and  $f_0$ ) relate the GTN model (see Section 2.1). These eight parameters represent specific values that modify an FE simulation result. The goal is to find an array of parameter values that, when comparing FE simulation results to a physical experiment result, have a low error. In other words we aim to find the array of parameter values that result in simulated output that agrees well with experimental data.

The term ‘parameter space’ is used to define the boundary within which our problem has a solution. That is to say each searchable parameter is defined in terms of its minimum and maximum value. This constitutes the space within which the BO algorithm will search for relevant values. The boundary of our problem is defined in Table 1. The minimum value of parameter  $m$  was assumed to be zero. A  $m = 0$  condition is representative of

perfectly plastic behaviour where true stress neither increases nor decreases as a function of true strain. The maximum value of parameter  $m$  was ascertained from experimental data. The process used to define parameter  $m$  is outlined in detail in Section 4. The minimum and maximum parameter values for the GTN model were selected from literature studies [31, 32], with modifications based on Abaqus limitations [24].

Table 1: Parameter space for P01 material. Note GTN parameters were assumed to be relevant to all material datasets. Parameter  $m$  was calculated from experimental data for each dataset. Datasets 1 & 2 were tested at room temperature (20 °C), Dataset 3 represents a high temperature test (500 °C).

Dataset	Parameter	Minimum	Maximum
1-3	$q_1$	0.90	1.60
1-3	$q_2$	0.90	1.10
1-3	$q_3$	0.81	2.56
1-3	$\epsilon_N$	0.25	0.40
1-3	$f_N$	0.03	0.09
1-3	$s_N$	0.10	0.20
1-3	$f_0$	0.0013	0.0015
1	$m$	0.00	800
2	$m$	0.00	1100
3	$m$	0.00	800



One of the key inputs to a BO process is a database of initial evaluated data. We use a design of experiment (DoE) approach to evaluate a limited number of positions within our parameter space. DoE is a method used

Table 2: Design of experiments array for 8 parameters with each parameter at 2 levels.

	$P_1$	$P_2$	$P_3$	$P_4$	$P_5$	$P_6$	$P_7$	$P_8$
<b>1</b>	1	1	1	1	1	1	1	1
<b>2</b>	1	1	1	1	1	2	2	2
<b>3</b>	1	1	2	2	2	1	1	1
<b>4</b>	1	2	1	2	2	1	2	2
<b>5</b>	1	2	2	1	2	2	1	2
<b>6</b>	1	2	2	2	1	2	2	1
<b>7</b>	2	1	2	2	1	1	2	2
<b>8</b>	2	1	2	1	2	2	2	1
<b>9</b>	2	1	1	2	2	2	1	2
<b>10</b>	2	2	2	1	1	1	1	2
<b>11</b>	2	2	1	2	1	2	1	1
<b>12</b>	2	2	1	1	2	1	2	1


~~predominately in manufacturing environments~~ to gain significant statistical information from fewer experiments [33, 34]. In this work the purpose of the DoE is to generate sufficient statistical data related to the black-box function  in as few simulations as possible. Table 2 shows a DoE array for 12 initial simulations based on the maximum and minimum parameter space values.

Figure 3 shows a flowchart describing the DoE procedure. The user defines the parameter space. A ~~generic~~ DoE array, such as that shown in Table 2, is ~~read into the system~~. The DoE array is then modified so that the ~~generic~~ minimum and maximum values (i.e. 1 for minimum and 2 for

maximum) are replaced by the user-defined parameter space values. We then conduct a FE simulation for each row of the ~~modified~~ DoE array. Results from the simulation are processed to **gather information similar to that of our physical experiment**. The physical experiment data are compared to the simulation data, and an error measurement is calculated (see Section 6 for further detail). After each iteration parameter values and the associated error measurement are appended to a csv file.

The output of the DoE (a csv file of parameter values and error measurements, Figure 3) is used to initialise the BO framework. Figure 4 outlines the BO framework. DoE data are analysed by the GPR to create an initial surrogate model. GPR outputs are provided to the acquisition function which identifies new parameter values based on ranking the DoE data. A new simulation, using acquisition function parameter values, is then conducted. Again simulation data is compared to the experiment and an error calculated. Acquisition function parameter values and error measurement data are appended to the existing csv file. As shown in Figure 4 the algorithm will iterate until either an appropriate solution is found (i.e. error of less than 2 % when comparing simulated and experimental results) or a maximum number of iterations (user-defined) is achieved.

### 3.1. The covariance function

The covariance function used in Bayesian optimization has significant influence on the shape and characteristics of the surrogate function [7]. ~~Simply put~~ the covariance function is a measure of how similar, or dissimilar, evaluation points are compared to their respective input positions. ~~Rasmussen and Williams [27] states that “it is a basic assumption that points with inputs~~

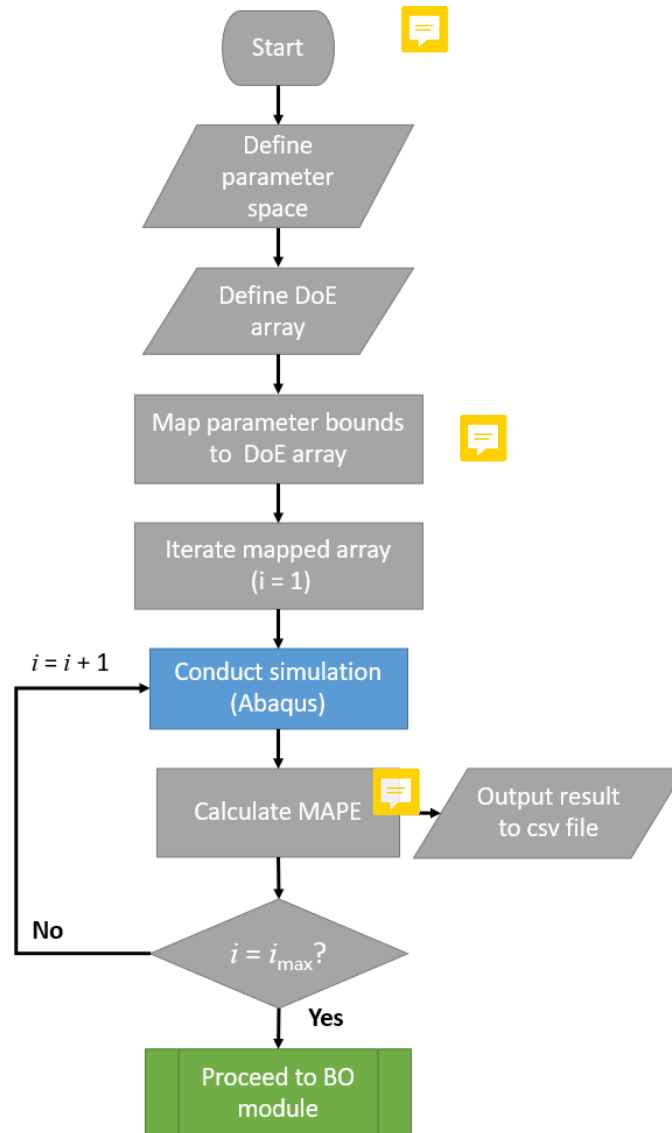


Figure 3: Flowchart demonstrating the design of experiments code procedure (prior to bayesian optimization). The output is a csv file of parameter values and associated error measurements.



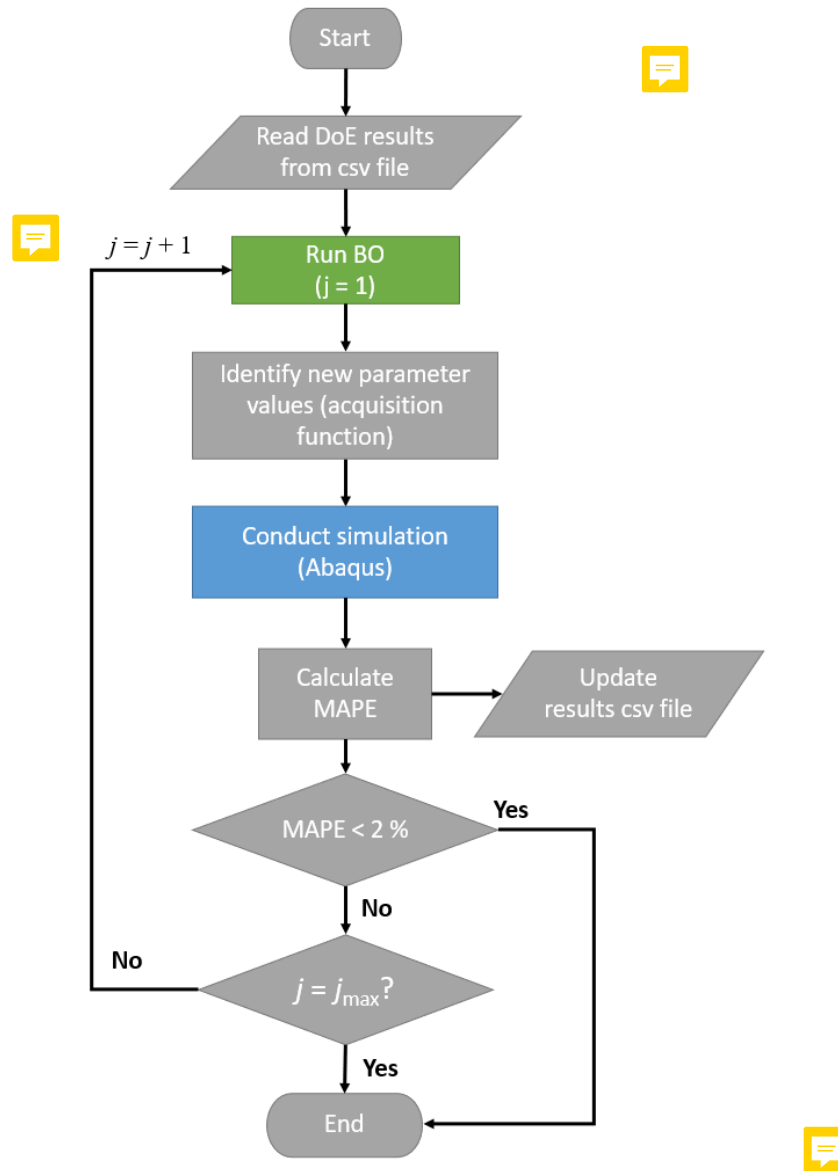


Figure 4: Flowchart depicting code procedure for Bayesian optimization. The optimiser uses information from design of experiments (Figure 3) to assess the relationship between parameter values and MAPE.

~~*x which are close are likely to have similar target values  $y$*~~ . In this work we employ a covariance function created from a combination of the Matérn, constant and white noise functions as shown in Equation 7.

$$k = \text{Matérn} + \text{Constant} \times \text{White} \quad (7) \quad \text{💬}$$

The Matérn covariance function is defined in Equation 8 [35], where  $d(\cdot, \cdot)$  is the Euclidean distance,  $K_\nu(\cdot)$  is a modified Bessel function and  $\Gamma(\cdot)$  is the gamma function. This type of covariance function is a generalisation of the radial basis function (RBF) with an additional parameter  $\nu$  controlling the smoothness of the function. When  $\nu \rightarrow \infty$  the covariance is equivalent to that of the RBF function, when  $\nu \rightarrow 0.5$  the covariance is identical to the absolute exponential covariance.

$$k(x_i, x_j) = \frac{1}{\Gamma(\nu) 2^{\nu-1}} \left( \frac{\sqrt{2\nu}}{l} d(x_i, x_j) \right)^\nu K_\nu \left( \frac{\sqrt{2\nu}}{l} d(x_i, x_j) \right) \quad (8)$$

To modify the mean of the Gaussian process we use the Constant covariance function see Equation 9 [35].

$$k(x_1, x_2) = \text{constant value} \forall x_1, x_2 \quad (9)$$

The white covariance function allows users to more accurately model noisy data. ~~Essentially~~ it is a squared exponential function with a short lengthscale. The main use of the White covariance function is to explain noise in the signal as an independent entity that is normally-distributed [35], Equation 10

$$k(x_1, x_2) = \text{noise level if } x_i == x_j \text{ else } 0 \quad (10) \quad \text{💬}$$

As we do not know the shape or characteristics of the black-box function our covariance kernel (Equation 7) is designed to account for shifts in mean position, noise and model potentially multiple minima positions.

### 3.2. The acquisition function

There are a number of methods that can be applied to identify new parameter values. In this work we have used the upper confidence bound (UCB). The UCB is considered an optimistic strategy given that parameters are identified through a weighted sum of the surrogate function  $\mu(x)$  and the uncertainty  $\sigma(x)$  [25, 36] as shown in Equation 11.



$$\alpha_{UCB}(x) = \mu(x) + \sqrt{B_t} \sigma(x) \quad (11)$$

When the weight  $(\sqrt{B_t})$  is large the model operates in exploratory mode, reducing the weight switches the model to exploitation mode. Exploration and exploitation balance how the model searches the parameter space. Exploration investigates inputs that are relatively far from one another. Exploitation assumes that you have located a ‘good’ result and now wish to search smaller distances from that point to identify the ‘best’ result. In BO one typically starts in exploration mode before moving to exploitation. The trade-off between exploration and exploitation is two-fold. Firstly it ensures that the model produces results in a reasonable timescale but secondly, and somewhat more importantly, the trade-off ensures the model doesn’t fall into a local minima.

Here we are trying to minimise the difference between simulated and experimental data where simulated data is a function of parameter values.

The objective is to identify the global minimum position of our unknown function  $f(x)$ . Essentially the weight value applied in Equation 11 controls the magnitude of ‘x’ relative to your current position. In our case the next ‘x’ position is an array of 8 parameter values. Given the complexity of the GTN model in terms of parameter dependencies we reduced the BO framework complexity by fixing  $B_t = 2.5$ .

#### 4. Experimental Tensile Tests

~~Tensile specimens were manufactured from ex-service P91 material and tested at temperatures of 20 °C and 500 °C. Specimens were manufactured by wire electro-discharge machining (EDM) and computer numerical control (CNC) machining. Room temperature testing was conducted on an Instron 8800 on two specimens. Testing conducted at 500 °C was carried out using a Tinius Olsen high-temperature test rig at a strain rate of 0.025 %/sec [32].~~ The three experimental tensile test results are shown in Figure 5. ~~Each tensile test result was analysed automatically using a python script. Test machine load-displacement data were converted to true stress-strain by first limiting data to the range below the maximum achieved load ( $P_{max}$ ) and then applying analytical solutions.~~ The ultimate tensile strength ( $\sigma_{UTS}$ ) was defined as the true stress corresponding to the position of  $P_{max}$ . ~~Data were linearly interpolated to increase the measurement density.~~ The second derivative of true strain was calculated using a  savitzky-golay filter with a three degree  polynomial fit. To ensure the yield strength was accurately defined the size of the filter window (i.e. the number of data points over which the polynomial is applied) was solved iteratively. For each iteration (i.e. each window size)

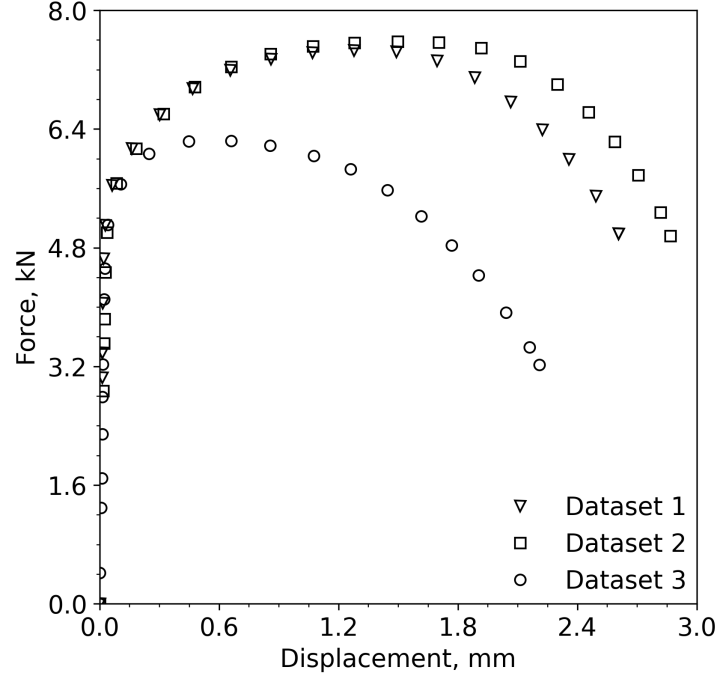


Figure 5: Experimental tensile test results for P91 material at test temperatures of 20 °C (Datasets 1 and 2) and 500 °C (Dataset 3). Note: Markers are placed as specific intervals for data visibility purposes. Higher data acquisition rate was used during testing.

the yield strength ( $\sigma_y$ ) was defined as the position of the inflection point. The ‘best’ yield strength was selected as a function of the error (between the predicted linear region and the experimental linear region), the overall fit of the linear region ( $r^2$ ) and the estimated yield strength value. Young’s modulus was calculated by employing linear regression to fit all data below the proposed ‘best’ yield strength. Figure 6 shows the result of the assessment for each of the three datasets.

To extrapolate data beyond  $\sigma_{UTS}$  a linear relationship between stress and strain was assumed. The slope of the extrapolated line, parameter  $m$ , is a

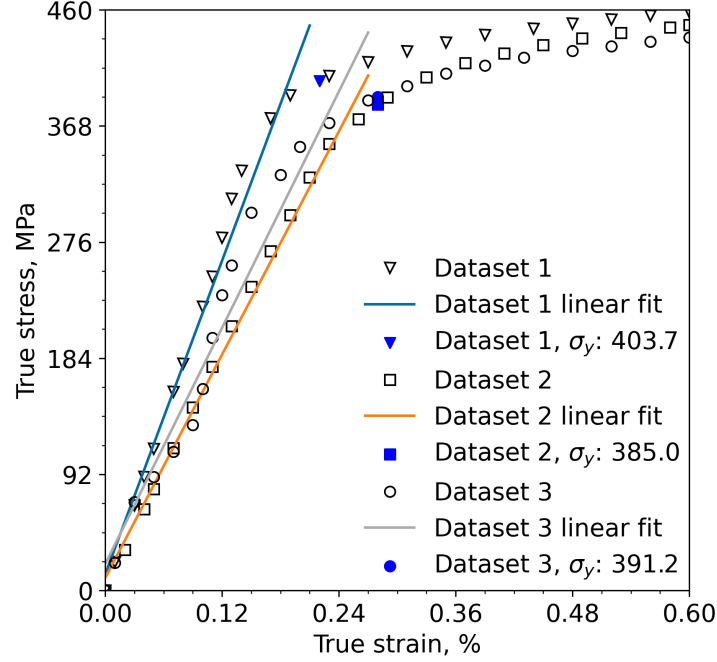


Figure 6: True stress - true strain relationship for three experimental tests. ~~Yield strength was identified using an iterative processes based on inflection points from the second derivative of strain.~~

searchable parameter that the BO framework will derive. ~~However, we must define the parameter space in terms of a minimum and maximum value. Here we assume that the minimum value of parameter  $m$  is zero. This is analogous to perfectly plastic material behaviour.~~ The maximum value of parameter  $m$  was ascertained from experimental data by applying a linear fit to groups of data preceeding the  $\sigma_{UTS}$  position. The first fit was applied to a single pair of data points immediately adjacent to the  $\sigma_{UTS}$  position, the second fit was applied to the previous pair plus an additional data point, the third fit was applied by expending the second group by an additional data point and so on. This method was applied up to a maximum of five data points preceding

the  $\sigma_{UTS}$  position. Parameter  $m$  was assessed for each linear fit and the largest value was selected to represent the maximum parameter boundary. True stress-true strain data were extrapolated based on the assumption that the extrapolated line must pass through the  $\sigma_{UTS}$  position with a slope of parameter  $m$ . Figure 7 shows the extrapolated data for the parameter space of dataset 1.

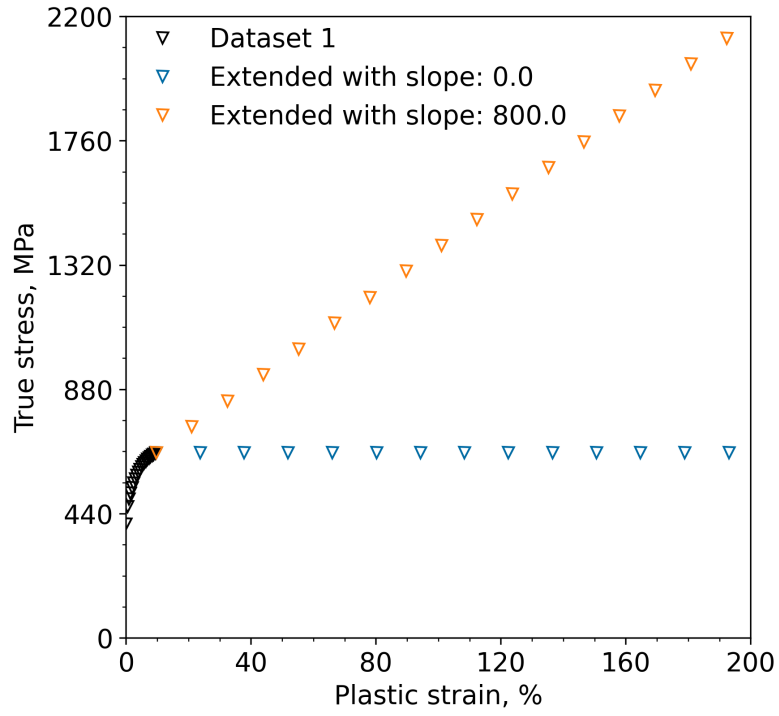


Figure 7: True stress - plastic strain relationship for dataset 1. Test data are shown using black markers. Data were extended beyond the ultimate tensile strength assuming a linear relationship for a range of parameter values. Two parameter values (the minimum and maximum) are plotted, these are distinguished using coloured markers.

## 5. FE Modelling of Tensile Tests

Finite element modelling was conducted using Abaqus 2021 [24]. Analyses were conducted using Abaqus/Explicit, a dynamics based solution, with a mass scaling factor of 10 to reduce computation time. The model was meshed using axisymmetric elements of type CAX4R, with a global mesh size of 0.1, applying a quadratic structured mesh strategy. A total of 4664 elements were used. Each element in the gauge section represents approximately 0.09 mm of specimen geometry.

The experimental tensile test geometry was represented as a 2D axisymmetric model as shown in Figure 8. The use of a 2D geometry reduces the computational expensive associated with the simulation. In turn, this allows us to increase the number of elements used to analyse the specimen increasing the accuracy of the result. Failure during experimental tensile testing most often occurs in the central region of the gauge length of the specimen. To predispose the FE model to failure in the central gauge length a small imperfection was introduced to the bottom right hand corner as shown in Figure 8.

Boundary conditions were applied along the symmetry planes (shown by the red dashed lines in Figure 8). Nodes along the x-plane were fixed in the vertical position ( $U_2=0$ ). A reference node (red point shown in Figure 8) was kinematically coupled to the surface of the geometry and loading was applied through displacement control. The maximum displacement applied represented the displacement at failure of the experimental test and was applied smoothly over the duration of the simulation.

The treatment of material data and the method of extrapolation are de-



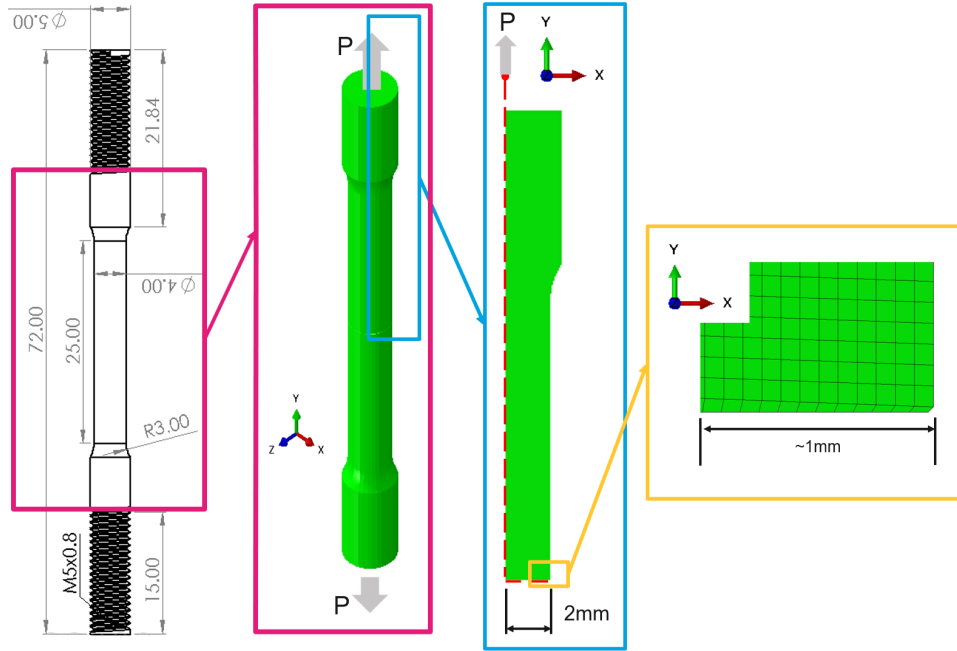


Figure 8: Illustration demonstrating the axisymmetric FE model. A small imperfection, shown in the yellow highlighted region, was modelled to ensure failure occurred in the midsection of the gauge length.

defined in Section 4. Within the FE simulation linear material behaviour was defined using the Young's modulus and Poisson's Ratio ( $\nu = 0.3$ ). Plastic material behaviour was provided as an array of plastic strain versus true stress. To more accurately model material degradation due to ductile damage the Gurson Tvergaard Needleman (GTN) material model was applied (see Section 2.1).

Simulation results were extracted using a python script. Displacement data was taken from the reference node shown in Figure 8. The applied load was calculated by summing the vertical reaction force (RF2) in elements located along the X symmetry plane.

## 6. Comparing experimental and simulated data

Mean average percentage error (MAPE), Equation 12, was used to measure similarity between the simulated output and experimental data. ~~Firstly we find the minimum change in displacement ( $\Delta u_{min}$ ) in either the experimental or simulated result. We then interpolate both arrays assuming a cubic relationship with an increment of  $\Delta u_{min}$ . This ensures that both simulated and experimental data have identical displacement arrays.~~ MAPE is calculated based on how similar the applied loading is for each increment of displacement as shown in Equation 12.

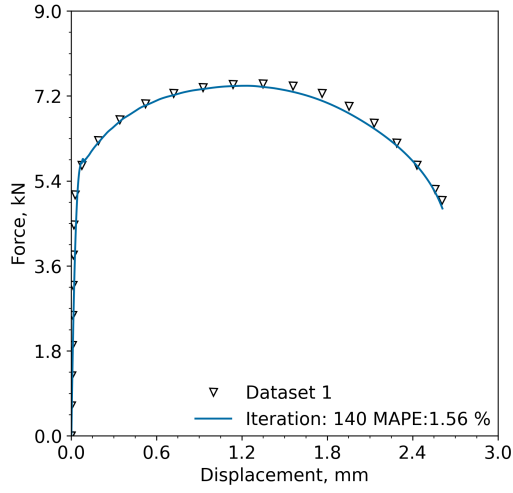
$$\text{MAPE} = \frac{100}{n} \sum \left| \left[ \frac{P_{exp} - P_{sim}}{P_{exp}} \right] \right| \quad (12)$$

MAPE provides an average measure of error over the data. In this work we have assumed that data points are equally weighted.

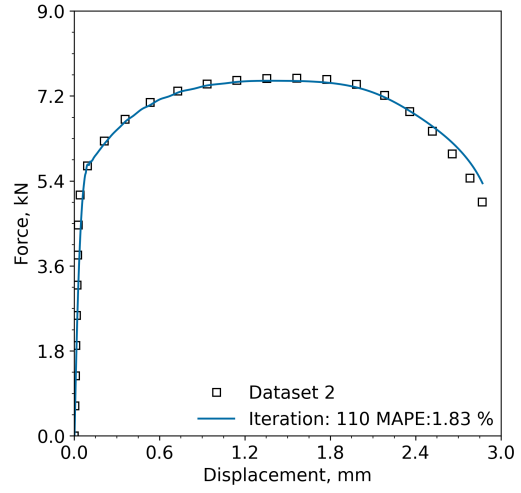
## 7. Results and Discussion

The parameter values selected by the BO framework are provided in Table 3 for each of the three datasets analysed. Simulated data, based on the parameter values shown in Table 3, are compared to the relevant experimental data in Figure 9 and, as shown, excellent agreement to experimental data was found for all datasets. In all cases the MAPE was found to be less than 2 %. The lowest MAPE, 1.56 %, was found for dataset 1.

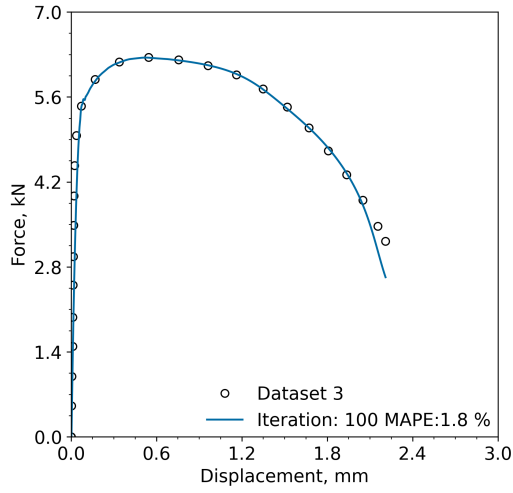
Figure 9a shows simulated output in good agreement with experimental data for comparable displacement values ~~excepting the~~ range  $1.3 \leq \Delta u \leq 2.2$  mm ~~where~~ simulated forces are slightly underestimated compared with



(a) Dataset 1



(b) Dataset 2



(c) Dataset 3

Figure 9: Comparison of experimental test data to simulated output for Dataset 1 (9a), Dataset 2 (9b), and Dataset 3 (9c). Parameter values are shown in Table 3.

Table 3: Bayesian optimisation framework parameter values for each of the three datasets analysed.

Parameter	Dataset 1	Dataset 2	Dataset 3
$q_1$	1.33244	1.16841	1.18197
$q_2$	0.99523	0.96665	0.96988
$q_3$	2.29488	1.40713	2.00065
$\epsilon_N$	0.29000	0.34674	0.37195
$s_N$	0.16706	0.18562	0.12137
$f_N$	0.03869	0.08481	0.04706
$f_0$	0.00137	0.00134	0.00131
$m$	534.13	725.39	421.41
MAPE	1.56	1.83	1.80
Iteration number	140	110	100

the experiment. Similarly Dataset 2 (Figure 9b) shows excellent agreement between simulated and experimental data up to a displacement of  $\approx 2.5$  mm. For  $\Delta u \geq \approx 2.5$  mm simulated results for Dataset 2 slightly overestimate the force compared to the experiment. The overestimation is most notable at the final displacement position. In general datasets 1 & 2, which were both room temperature tests, are excellent representations of the experimental data. It is interesting to note that parameter  $m$ , the slope of the extrapolated true stress-true strain curve was found to differ significantly. The optimised parameter  $m$  for Datasets 1 was found to be 534.13 MPa while that for Dataset 2 was found to be 725.39 MPa. Both Datasets were tested under

identical conditions and, as shown in Figure 5, are broadly similar up to a displacement of  $\approx 1.3$  mm after which they begin to diverge. It is clear from Figure 5 that Dataset 2 **degrades** at a faster rate compared to Dataset 1. As specified in Section 4, the extrapolation method inherently assumes that the linear fit must pass through the  $\sigma_{UTS}$  position. At the  $\sigma_{UTS}$  position,  $\Delta u \approx 1.4$  mm there is already a notable difference in force when comparing Datasets 1 & 2. This implies that manually fitting linear extrapolations to these two datasets would cause the slope of the extrapolated line (i.e. parameter  $m$ ) to differ substantially. Thus we can conclude that while the difference in parameter  $m$  is initially surprising it follows a logical process.

~~The third dataset (Dataset 3, Figure 9c) represents a high temperature test conducted at 500 °C. In Figure 5 we showed that the high temperature test differs significantly compared to room temperature tests. This is as expected given that increasing test temperature introduces additional kinetic energy at an atomic level which directly affects both the yield strength and flow stress of the material. Figure 9c shows excellent agreement with experimental data was achieved for displacements  $\leq \approx 2$  mm. At larger displacements,  $\Delta u \geq 2$  mm the simulated degrades at a faster rate compared to the experiment.~~

It is interesting to note that for all three datasets the parameter  $f_0$ , representing the initial void volume fracture of the material, are similar but not identical. Parameter  $f_0$  can be defined experimentally [21, 22, 37] but experimental values vary widely due to the subjective nature of the assessment. For example, Gülçimen Çakan et al. [21] conducted an experiment on P91 material and found  $f_0$  to have a range of  $0.0044 \geq f_0 \leq 0.002$ . In FE assess-

ments Gülcimen Çakan et al. [21] noted that  $f_0$  had only a marginal effect on simulated output up to the ultimate tensile strength ( $\sigma_{UTS}$ ) but a significant affect beyond this point with larger values of  $f_0$  resulting in earlier failure. Gülcimen Çakan et al. [21] found that simulated output with  $f_0 = 0.0044$  provided better agreement with experimental data though this was based on a single experimental test result. It is not clear whether the value of  $f_0$  would remain appropriate for additional tests.

Generally the initial void volume fraction is assumed to be applicable to all test samples taken from a single piece of material. This is, at least in part, due to the difficulty in assigning a parameter value. The statistical nature of materials testing, often termed material scatter, has been widely acknowledged in the field of material science [38]. Given the difficulty in experimentally deriving appropriate  $f_0$  values and considering the statistical nature of material performance, it may be that machine learning methods like that employed here are more appropriate for defining this parameter. Essentially using machine learning, as it is employed here, results in a specimen specific parameter for  $f_0$ . The lack of identical parameter  $f_0$  values seen here are considered a reflection of the expected scatter behaviour seen in the wider field.

Comparing parameters  $\epsilon_N$ ,  $S_N$  and  $f_N$  across the three datasets presented in Table 3 show relatively significant changes when comparing any given parameter. While one might expect the fraction of nucleated voids,  $f_N$ , to be specimen specific the remaining parameters  $\epsilon_N$  and  $S_N$  are not expected to be such.  $\epsilon_N$  and  $S_N$  represent the mean and standard deviation, respectively, associated with a normally distributed curve. These parameters essentially

control how many voids nucleate under a given loading condition. As such parameters  $\epsilon_N$  and  $S_N$  are considered material specific rather than specimen specific. Given the complex nature of the material model and the close relationship between these parameters it is difficult to state with any certainty what impact any given parameter has had on simulated output.

## 8. Conclusions

- Bayesian optimization framework successfully derived an array of 8 parameter values that, when applied to a ductile damage model simulation, produced an accurate representation of experimental data with a mean average percentage error of less than 2 %.
- The framework is fully autonomous requiring only basic information that can be easily generated from experimental tensile test data.
- ~~Parameters selected by the BO framework do not result in good agreement when the analyses are conducted using Abaqus implicit solver.~~

Data files and code used in this paper can be downloaded from [https://github.com/alisonoc/PAPER\\_A](https://github.com/alisonoc/PAPER_A).

## 9. Acknowledgements

This work was funded by the European Union through the Marie Skłodowska-Curie Actions grant number 101028291. William Brennan, a University of Limerick undergraduate, is thanked for his contributions to earlier versions of the algorithm used in this work. We gratefully acknowledge helpful conversations with Dr. Meghana Kshiragar and Gauri Vaidya from the University

of Limerick’s Lero Centre. We also thank the Mathematics Applications Consortium for Science and Industry (MACSI) group for their insightful and supportive comments surrounding this research.

## References

- [1] T. L. Anderson, Fracture Mechanics: Fundamentals and Applications, Boca Raton, FL: Taylor & Francis, 2005.
- [2] D. L. Logan, A First Course in the Finite Element Method, CL Engineering; Cengage Learning, 2016.
- [3] J.-Y. Wu, V. P. Nguyen, C. T. Nguyen, D. Sutula, S. Sinaie, S. Bordas, Phase-field modeling of fracture, in: Advances in Applied Mechanics, Elsevier, 2019/12/18/.
- [4] F. Abbassi, T. Belhadj, S. Mistou, A. Zghal, Parameter identification of a mechanical ductile damage using Artificial Neural Networks in sheet metal forming, Materials & Design 45 (2013) 605–615. doi:<http://dx.doi.org/10.1016/j.matdes.2012.09.032>.
- [5] Y. Chahboub, S. Szavai, Determination of GTN parameters for SENT specimen during ductile fracture, in: Procedia Structural Integrity, volume 16, Elsevier B.V., 2019, pp. 81–88. doi:[10.1016/j.prostr.2019.07.025](http://dx.doi.org/10.1016/j.prostr.2019.07.025).
- [6] T. Zhang, K. Lu, A. Mano, Y. Yamaguchi, J. Katsuyama, Y. Li, A novel method to uniquely determine the parameters in Gur-



- son–Tvergaard–Needleman model, *Fatigue & Fracture of Engineering Materials & Structures* 44 (2021) 3399–3415. doi:[10.1111/ffe.13568](https://doi.org/10.1111/ffe.13568).
- [7] P. G. Mongan, V. Modi, J. W. McLaughlin, E. P. Hinchy, R. M. O’Higgins, N. P. O’Dowd, C. T. McCarthy, Multi-objective optimisation of ultrasonically welded dissimilar joints through machine learning, *Journal of Intelligent Manufacturing* 33 (2022) 1125–1138. doi:[10.1007/s10845-022-01911-6](https://doi.org/10.1007/s10845-022-01911-6).
- [8] X. Liu, C. E. Athanasiou, N. P. Padture, B. W. Sheldon, H. Gao, A machine learning approach to fracture mechanics problems, *Acta Materialia* 190 (2020) 105–112. doi:[10.1016/j.actamat.2020.03.016](https://doi.org/10.1016/j.actamat.2020.03.016).
- [9] J. Hegde, B. Rokseth, Applications of machine learning methods for engineering risk assessment – A review, *Safety Science* 122 (2020) 104492. doi:[10.1016/j.ssci.2019.09.015](https://doi.org/10.1016/j.ssci.2019.09.015).
- [10] J. Snoek, H. Larochelle, R. P. Adams, Practical Bayesian Optimization of Machine Learning Algorithms, in: *Advances in Neural Information Processing Systems*, volume 25, Curran Associates, Inc., 2012.
- [11] I. Dewancker, M. McCourt, S. Clark, Bayesian Optimization for Machine Learning : A Practical Guidebook, arXiv:1612.04858 [cs] (2016). [arXiv:1612.04858](https://arxiv.org/abs/1612.04858).
- [12] T. Bismukhametov, J. Jäschke, Combining machine learning and process engineering physics towards enhanced accuracy and explainability of data-driven models, *Computers & Chemical Engineering* 138 (2020) 106834. doi:[10.1016/j.compchemeng.2020.106834](https://doi.org/10.1016/j.compchemeng.2020.106834).

- [13] F. Ghavamian, Accelerating finite element analysis using machine learning (2021). doi:[10.4233/uuid:015bbf35-5e29-4630-b466-1a29d4c5bfb3](https://doi.org/10.4233/uuid:015bbf35-5e29-4630-b466-1a29d4c5bfb3).
- [14] M. Jokar, F. Semperlotti, Finite element network analysis: A machine learning based computational framework for the simulation of physical systems, *Computers & Structures* 247 (2021) 106484. doi:[10.1016/j.compstruc.2021.106484](https://doi.org/10.1016/j.compstruc.2021.106484).
- [15] L. Zhang, L. B. Jack, A. K. Nandi, Fault detection using genetic programming, *Mechanical Systems and Signal Processing* 19 (2005) 271–289. doi:[10.1016/j.ymssp.2004.03.002](https://doi.org/10.1016/j.ymssp.2004.03.002).
- [16] C. C. Aggarwal, *Neural Networks and Deep Learning*, Springer International Publishing, 2018. doi:[10.1007/978-3-319-94463-0](https://doi.org/10.1007/978-3-319-94463-0).
- [17] S. Ryan, J. Berk, S. Rana, B. McDonald, S. Venkatesh, A bayesian optimisation methodology for the inverse derivation of viscoplasticity model constants in high strain-rate simulations, *Defence Technology* (2021). doi:[10.1016/j.dt.2021.10.013](https://doi.org/10.1016/j.dt.2021.10.013).
- [18] M. Abendroth, M. Kuna, Identification of ductile damage and fracture parameters from the small punch test using neural networks, *Engineering Fracture Mechanics* 73 (2006) 710–725. doi:[10.1016/j.engfracmech.2005.10.007](https://doi.org/10.1016/j.engfracmech.2005.10.007).
- [19] D. Chen, Y. Li, X. Yang, W. Jiang, L. Guan, Efficient parameters identification of a modified GTN model of ductile fracture using machine

- learning, *Engineering Fracture Mechanics* 245 (2021) 107535. doi:[10.1016/j.engfracmech.2021.107535](https://doi.org/10.1016/j.engfracmech.2021.107535).
- [20] A. Pineau, A. A. Benzerga, T. Pardoen, Failure of metals I: Brittle and ductile fracture, *Acta Materialia* 107 (2016) 424–483. doi:[10.1016/j.actamat.2015.12.034](https://doi.org/10.1016/j.actamat.2015.12.034).
- [21] B. Gülçimen Çakan, C. Soyarslan, S. Bargmann, P. Hähner, Experimental and Computational Study of Ductile Fracture in Small Punch Tests, *Materials* 10 (2017) 1185. doi:[10.3390/ma10101185](https://doi.org/10.3390/ma10101185).
- [22] W. Wcislik, Experimental determination of critical void volume fraction  $f_F$  for the Gurson Tvergaard Needleman (GTN) model, *Procedia Structural Integrity* 2 (2016) 1676–1683. doi:[10.1016/j.prostr.2016.06.212](https://doi.org/10.1016/j.prostr.2016.06.212).
- [23] V. Tvergaard, A. Needleman, Analysis of the cup-cone fracture in a round tensile bar, *Acta Metallurgica* 32 (1984) 157–169. doi:[10.1016/0001-6160\(84\)90213-X](https://doi.org/10.1016/0001-6160(84)90213-X).
- [24] D. Systemes, Abaqus/CAE User’s Guide - SIMULIA User Assistance 2021, Dassault Systemes, 2021.
- [25] B. Shahriari, K. Swersky, Z. Wang, R. P. Adams, N. de Freitas, Taking the Human Out of the Loop: A Review of Bayesian Optimization, *Proceedings of the IEEE* 104 (2016) 148–175. doi:[10.1109/JPROC.2015.2494218](https://doi.org/10.1109/JPROC.2015.2494218).
- [26] C. E. Rasmussen, Gaussian Processes in Machine Learning, in: O. Bousquet, U. von Luxburg, G. Rätsch (Eds.), *Advanced Lectures on Machine*

- Learning: ML Summer Schools 2003, Canberra, Australia, February 2 - 14, 2003, Tübingen, Germany, August 4 - 16, 2003, Revised Lectures, Lecture Notes in Computer Science, Springer, Berlin, Heidelberg, 2004, pp. 63–71. doi:[10.1007/978-3-540-28650-9\\_4](https://doi.org/10.1007/978-3-540-28650-9_4).
- [27] C. E. Rasmussen, C. K. I. Williams, Gaussian Processes for Machine Learning, Adaptive Computation and Machine Learning, MIT Press, Cambridge, Mass, 2006.
  - [28] J. Wang, An Intuitive Tutorial to Gaussian Processes Regression, 2022. [arXiv:2009.10862](https://arxiv.org/abs/2009.10862).
  - [29] D. Duvenaud, Automatic Model Construction with Gaussian Processes, Thesis, University of Cambridge, 2014. doi:[10.17863/CAM.14087](https://doi.org/10.17863/CAM.14087).
  - [30] A. Caliskan, M. E. Yuksel, H. Badem, A. Basturk, Performance improvement of deep neural network classifiers by a simple training strategy, Engineering Applications of Artificial Intelligence 67 (2018) 14–23. doi:[10.1016/j.engappai.2017.09.002](https://doi.org/10.1016/j.engappai.2017.09.002).
  - [31] R. Kiran, K. Khandelwal, Gurson model parameters for ductile fracture simulation in ASTM A992 steels, Fatigue & Fracture of Engineering Materials & Structures 37 (2014) 171–183. doi:[10.1111/ffe.12097](https://doi.org/10.1111/ffe.12097).
  - [32] E. D. Meade, Experimental Study & Multiscale Modelling of the High Temperature Deformation of P91 under Multiaxial Loading, Ph.D. thesis, University of Limerick, 2020.
  - [33] M. Uy, J. K. Telford, Optimization by Design of Experiment techniques,

- in: 2009 IEEE Aerospace Conference, 2009, pp. 1–10. doi:[10.1109/AERO.2009.4839625](https://doi.org/10.1109/AERO.2009.4839625).
- [34] S. Fraley, M. Oom, B. Terrien, J. Zalewski, 14.1: Design of Experiments via Taguchi Methods - Orthogonal Arrays, in: Chemical Process Dynamics and Controls, 2020.
- [35] F. Pedregosa, G. Varoquaux, A. Gramfort, V. Michel, B. Thirion, O. Grisel, M. Blondel, P. Prettenhofer, R. Weiss, V. Dubourg, J. Vanderplas, A. Passos, D. Cournapeau, M. Brucher, M. Perrot, É. Duchesnay, Scikit-learn: Machine Learning in Python, *Journal of Machine Learning Research* 12 (2011) 2825–2830.
- [36] G. De Ath, R. M. Everson, A. A. M. Rahat, J. E. Fieldsend, Greed is Good: Exploration and Exploitation Trade-offs in Bayesian Optimisation, *ACM Transactions on Evolutionary Learning and Optimization* 1 (2021) 1–22. doi:[10.1145/3425501](https://doi.org/10.1145/3425501). [arXiv:1911.12809](https://arxiv.org/abs/1911.12809).
- [37] W. Brocks, D. Klingbeil, G. Künecke, D.-Z. Sun, Application of the Gurson Model to Ductile Tearing Resistance, in: A. Bakker (Ed.), *Constraint Effects in Fracture Theory and Applications: Second Volume*, ASTM International, West Conshohocken, PA, 1995, pp. 232–252. doi:[10.1520/STP14638S](https://doi.org/10.1520/STP14638S).
- [38] A. N. O’Connor, C. M. Davies, S. J. Garwood, The influence of constraint on fracture toughness: Comparing theoretical T<sub>0</sub> shifts in master curve analyses with experimental data, *Engineering Fracture Mechanics* 275 (2022) 108857. doi:[10.1016/j.engfracmech.2022.108857](https://doi.org/10.1016/j.engfracmech.2022.108857).